3-2021

Microwave-assisted modulation of light emission intensity in alkali-pyrotechnic plumes

Stuart J. Barkley
Iowa State University, stuartb@iastate.edu

Joel E. Lynch
Iowa State University, lynch@iastate.edu

Eric J. Miklaszewski
Naval Surface Warfare Center

Jonathan M. Dilger
Naval Surface Warfare Center

William F. Crespo
Naval Surface Warfare Center

See next page for additional authors

Microwave-assisted modulation of light emission intensity in alkali-pyrotechnic plumes

Abstract

Creating next-generation pyrotechnic emitters capable of dynamically controllable light output requires a paradigm shift away from emission control via formulation. This work demonstrates the ability to modulate light emission intensity of a pyrotechnic flame with 2.46 GHz microwave energy within a multimodal cavity. Stoichiometric mixtures of three pyrotechnic systems are investigated: magnesium fuel with oxidizers of $NaNO_3$, KNO_3, or $CsNO_3$. Using time-resolved visible and infrared emission spectroscopy and high-speed color videography, microwave illumination of flames is found to produce enhanced atomic photo emission from the alkali species. Emission increases of up to ~120% are demonstrated, which are predominantly in the visible and near-infrared wavelengths and have little effect on flame emission chromaticity. At near- and mid-IR wavelengths, gray body continuum enhancement is observed with moderate enhanced emission from CO_2 and H_2O bands. Sustained light emission from microwave illumination of combustion products long after pyrotechnic extinguishment was also demonstrated. A simplified model of microwave-enhanced visible and near-IR emission is presented and shown to be consistent with the observed trend of elevated emission enhancement for lower wavelength alkali transitions. Sensitivity analysis is performed which suggests a lower equilibrium population of electronically excited alkali atoms is primarily responsible for maximizing the degree of light emission enhancement of applied microwave fields, especially in extinguished low-temperature pyrotechnic plumes. These findings suggest microwave illumination of alkali-containing pyrotechnic flames may be a useful strategy to achieve dynamic control of light emission intensity.

Keywords

Pyrotechnics, Energetic materials, Metal combustion, Alkali metal-doping, Plasma-assisted combustion

Disciplines

Acoustics, Dynamics, and Controls | Heat Transfer, Combustion | Mechanical Engineering

Comments

This article is published as Barkley, Stuart J., Joel E. Lynch, Eric J. Miklaszewski, Jonathan M. Dilger, William F. Crespo, James B. Michael, Shankar Subramaniam, and Travis R. Sippel. "Microwave-assisted modulation of light emission intensity in alkali-pyrotechnic plumes." *Combustion and Flame* 225 (2021): 406-416. DOI: 10.1016/j.combustflame.2020.11.005.

Authors

Stuart J. Barkley, Joel E. Lynch, Eric J. Miklaszewski, Jonathan M. Dilger, William F. Crespo, James B. Michael, Shankar Subramaniam, and Travis R. Sippel

Combustion and Flame 225 (2021) 406–416

Contents lists available at ScienceDirect

Combustion and Flame

journal homepage: www.elsevier.com/locate/combustflame

Microwave-assisted modulation of light emission intensity in alkali-pyrotechnic plumes

Stuart J. Barkley[a,*], Joel E. Lynch[a], Eric J. Miklaszewski[b], Jonathan M. Dilger[b], William F. Crespo[b], James B. Michael[a], Shankar Subramaniam[a], Travis R. Sippel[a]

[a] Department of Mechanical Engineering, Iowa State University, 2025 Black Engineering Building, Ames, IA 50011, USA
[b] Naval Surface Warfare Center, Crane Division, Crane, IN 47522, USA

ARTICLE INFO

Article history:
Received 22 June 2020
Revised 5 November 2020
Accepted 5 November 2020

Keywords:
Pyrotechnics
Energetic materials
Metal combustion
Alkali metal-doping
Plasma-assisted combustion

ABSTRACT

Creating next-generation pyrotechnic emitters capable of dynamically controllable light output requires a paradigm shift away from emission control via formulation. This work demonstrates the ability to modulate light emission intensity of a pyrotechnic flame with 2.46 GHz microwave energy within a multimodal cavity. Stoichiometric mixtures of three pyrotechnic systems are investigated: magnesium fuel with oxidizers of $NaNO_3$, KNO_3, or $CsNO_3$. Using time-resolved visible and infrared emission spectroscopy and high-speed color videography, microwave illumination of flames is found to produce enhanced atomic photo emission from the alkali species. Emission increases of up to ~120% are demonstrated, which are predominantly in the visible and near-infrared wavelengths and have little effect on flame emission chromaticity. At near- and mid-IR wavelengths, gray body continuum enhancement is observed with moderate enhanced emission from CO_2 and H_2O bands. Sustained light emission from microwave illumination of combustion products long after pyrotechnic extinguishment was also demonstrated. A simplified model of microwave-enhanced visible and near-IR emission is presented and shown to be consistent with the observed trend of elevated emission enhancement for lower wavelength alkali transitions. Sensitivity analysis is performed which suggests a lower equilibrium population of electronically excited alkali atoms is primarily responsible for maximizing the degree of light emission enhancement of applied microwave fields, especially in extinguished low-temperature pyrotechnic plumes. These findings suggest microwave illumination of alkali-containing pyrotechnic flames may be a useful strategy to achieve dynamic control of light emission intensity.

1. Introduction

Microwave coupling to pyrotechnics provides an intriguing possibility for control of light emission, with applications including enhanced brightness battlefield illuminants, dynamically controlled strobe formulations, and 'smart' flares with dynamically controlled color or color ratio. Conventional strategies require tailoring the composition to include various colorant additives (e.g., nitrate salts of barium, sodium, or strontium), selection of formulations with unsteady combustion, or other methods to achieve the desired wavelength, color purity, and intensity [1]. This approach can be laborious and offers no real time control. Moreover, light-emission design through formulation can result in hazards, as many colorants and additives commonly used today (e.g., perchlorates, heavy-metals, strontium additives, and barium additives) produce toxic or environmentally hazardous products [2]. New strategies are needed for producing high color purity and high radiance emitters, while also reducing fabrication complexity and the use of hazardous or regulated emitter ingredients.

This proposed technique draws heavily from historical efforts to enhance and control hydrocarbon flames using sub-breakdown electric fields, a well-reviewed topic within plasma-assisted combustion research [3,4]. In particular, high-frequency electric fields (e.g., MHz and above at atmospheric pressures), have been used to improve igniters and enhance flame speed [3]. In these gas-phase systems, field energy is primarily deposited to free electrons, the only charged species able to gain and transfer momentum in phase with the alternating electric field. The intricate balance of electron heating and relaxation by atomic and molecular collisions is characterized by the Boltzmann equation, ultimately enabling non-equilibrium populations of excited state neutrals [5–7]. Herein, we refer to this approach as weak microwave induced plasma (WMIP), which is similar to conventional MIP but generated by relatively

* Corresponding author.
E-mail address: stuartb@iastate.edu (S.J. Barkley).

https://doi.org/10.1016/j.combustflame.2020.11.005
0010-2180/

Symbols

Experimental

E_e	relative spectral irradiance
$E_{e,\ total}$	time-integrated relative spectral irradiance
m_{sample}	pyrotechnic article mass
F_s	spectrometer sampling frequency
$T_{adiabatic}$	adiabatic pyrotechnic temperature
X_i, Y_i, Z_i	tristimulus values
$\bar{x},\ \bar{y}, \bar{z}$	CIE 1931 color-matching functions

Constants

ε_0	vacuum permittivity
m_e	electron mass
k_b	Boltzmann constant
h	Planck's constant

Two-level alkali emission

A_{21}	spontaneous emission rate
f_{12}	oscillator potential
$g_1,\ g_2$	alkali degeneracies
$\lambda,\ \lambda_{21}$	wavelength, line-center wavelength
$\nu,\ \nu_{21}$	frequency, line-center frequency
$N_1,\ N_2$	alkali number density, ground & excited state
ϕ_ν	spectral line shape function
$\Delta\nu$	line shape full width half max
k_ν	spectral absorption coefficient
τ	optical depth

Model

$\varepsilon(s)$	emission coefficient
$\mathcal{T}(s)$	optical transmittance
$E(s)$	RMS electric field
s	plume depth coordinate
δ	plume skin depth
L	maximum plume depth
$K_{M+},\ K_{M-}$	alkali-neutral rates
$K_{E+},\ K_{E-}$	electron-neutral rates
$P_1,\ P_2,\ P_3$	electron-alkali excitation quadratic coefficients
$Q_1,\ Q_2$	electron-alkali quenching coefficients
$X_e,\ X_{mol},\ X_{alk}$	electron, molecule, alkali mole fractions
σ_A	alkali-nitrogen quenching cross-section
μ_{eff}	alkali-nitrogen effective mass
α_0	plume attenuation coefficient
$\widetilde{\mu_0}$	plume complex index of refraction
$n_0,\ n_{amb}$	total number density, plume and ambient
T_0, T_{amb}	gas temperature, plume and ambient

weak (sub-breakdown) electric fields. For alkali-pyrotechnics, early research confirmed that visible and near-infrared (VIS/NIR) emission is dominated by spontaneous emission from electronically excited alkali atoms [8–12], making the WMIP approach relevant for these systems. While direct electron collisions are thought to be the primary pathway for producing excess alkali emitters, indirect production by collisions with other excited molecules, like electronically-excited metastable nitrogen, may play a role [13].

Beyond gas-phase flames, energetic materials and their multiphase products have demonstrated a variety of pathways for electric-field enhancement. Application of microwave fields to aluminized solid propellants containing low ionization energy dopants (e.g., $NaNO_3$ 16 wt.%) have been shown to increase the atmospheric pressure burning rate by up to 60%. The ability of the WMIP hypothesis to be applied to these materials was bolstered by direct measurements of non-equilibrium sodium temperatures [14]. Still, the burning rate enhancement of a propellant can also result from microwave energy transfer through other mechanisms, including (1) dielectric thermal runaway of metallic oxide combustion products [15], and (2) dielectric heating of the condensed-phase propellant reactants. Microwave energy transfer to condensed phase reactants of energetic materials containing electrically conductive phases (e.g., metal fuels) is expected to be higher due to eddy current heating [16], which, for metal spheres, is a function of the particle size and microwave penetration depth [17,18]. In order to improve microwave absorption of most non-metallized energetic materials [19–21], additives with high dielectric loss have been included [22,23].

While both the gaseous and condensed phases provide pathways for energy deposition via high-frequency fields, there are significant obstacles to realizing enhancement with microwaves. Chiefly, the microwave frequency range (~1–10 GHz) resides below typical plasma frequencies for adiabatic combustion of alkali pyrotechnics (~0.1–1 THz), which limits microwave penetration to the outer regions of pyrotechnic plumes where air entrainment reduces the temperature, alkali density, and electron density. Additionally, to sustain a non-equilibrium population of emitters, the electron-alkali excitation rate must exceed the efficient alkali-molecular quenching processes [24]. Finally, while the high concentrations of alkali species may be expected to yield substantial increases in the alkali atomic emission, this may be offset by self-absorption of emitted radiation which has been well documented in sodium lamps and alkali-pyrotechnics [8–12,25]. Self-absorption is mitigated by resonant atomic broadening, which shifts emission wavelengths to regions far from line center with less absorption [25]. Thus, the degree of light emission enhancement that can be expected from application of an electromagnetic field to an alkali pyrotechnic flame remains an open question.

Modeling of emission in alkali-magnesium pyrotechnics has been performed, but only under the strict conditions of Boltzmann (electronic), Saha (ionic), and Planck (optical) equilibrium [8–11]. Still, relaxing these assumptions has become commonplace in plasma modeling [26], and provides a framework for inclusion in pyrotechnic emission models. First, Boltzmann non-equilibrium, both in the electron and excited-state alkali species, must be accounted for. Rate coefficient data for alkali excitation and quenching in molecular gases is well known [24], and the rates of electron-alkali excitation and super-elastic collisions can be computed using a Boltzmann solver with the appropriate electron-alkali cross-section data [27]. Second, deviations from Saha equilibrium sufficient to cause electrical breakdown are possible but are not typically desired for free-space combustion enhancement. Finally, Planck non-equilibrium, the imbalance of absorption and emission, while inevitable, requires solution of the radiation-transfer equation.

Given the possible limitations of coupling microwaves to pyrotechnics, demonstrating the extent to which light emission can be augmented in alkali pyrotechnics is a critical task. Additionally, development of an initial model of WMIP enhancement for pyrotechnic emission is necessary to test this hypothesis and analyze the experimental results. Thus, we explore interactions of 2.46 GHz microwave energy with three magnesium-based pyrotechnics, each containing alkali nitrate oxidizers of sodium, potassium, or cesium. Small pyrotechnic articles are fabricated and burned inside of an 870 W, 60-Hz modulated, multimode microwave cavity. The effects of microwave illumination on flame emission are probed using optical diagnostics, including VIS/NIR and infrared (IR) emission spectroscopy, and color high-speed imaging in order to gain insight into the effects of microwave illumination on an alkali-pyrotechnic flame. These results are compared with a preliminary model for microwave enhancement in a model pyrotechnic plume, to determine the extent to which the WMIP pathway can replicate exper-

imental VIS/NIR emission enhancement. Additionally, perturbation analysis is used to identify a possible explanation for the variation in enhancement observed between alkali species.

2. Experimental and computational methods

2.1. Equilibrium chemical calculations

Chemical equilibrium calculations were conducted to identify ion and electron populations, adiabatic flame temperatures, and condensed-phase flame products in each alkali-nitrate formulation. The NASA Chemical Equilibrium with Applications (CEA) code [28] was used to make thermochemical predictions at sea-level atmospheric conditions (1 atm, 10 wt.% excess air). In these calculations, the assumed heat of formation of the epoxy binder (Epon/Versamid; $H_{98}C_{83}O_{14}N_4$) was −3666 kJ-mol^{-1}. All calculations were conducted with ion chemistry enabled.

2.2. Pyrotechnic manufacture

The pyrotechnic formulations used in this study consisted of magnesium (Firefox; 190–325 mesh), one of three different alkali nitrate oxidizers, and the aforementioned epoxy binder. All compositions were formulated for stoichiometric combustion in order to achieve maximum equilibrium flame temperatures. Alkali nitrate oxidizers used in formulations consisted of one of the following: sodium nitrate (Hummel Croton Inc., MIL-S-322C, Grade B, Mg/$NaNO_3$/epoxy: 45.6/49.4/5 wt.%); potassium nitrate (Hummel Croton Inc., MIL-P-156B, Mg/KNO_3/epoxy: 42.8/52.2.4/5 wt.%); or cesium nitrate (American Elements Engineering, Mg/$CsNO_3$/epoxy: 28.5/66.5/5 wt.%). The epoxy binder used was a two-part thermoset-epoxy consisting of 70 wt. % Epon-813 and 30 wt.% Versamid-140. All pyrotechnic compositions were hand-mixed in a grounded pan using a metal spatula in quantities of 10 g or less. First, the fuel and binder were hand-mixed until homogeneous. Oxidizer was then blended into the fuel/binder premixture. The composition was again hand-mixed until homogeneous. To achieve the desired consolidation density, reactive compositions were shim-pressed in a 6 mm diameter circular die to a nominal length of 9 mm using a Carver 12-ton press and a dwell time of approximately 10 s. Prior to combustion, pellets were inhibited with an acrylic lacquer to prevent flame spread down the sides of the pellet.

2.3. Microwave combustion cavity

A multimode microwave cavity (Fig. 1a) connected to an 870 W, ~2.46 GHz magnetron and a high-voltage power supply modulated at 60 Hz (50% duty cycle) was used for experiments. The pyrotechnic was placed in an electric-field (E-field) antinode atop a microwave-transparent polytetrafluoroethylene (PTFE) block. The location of the field antinode was verified both experimentally and by numerical simulation. Experimentally, the E-field antinode location was found by imaging a liquid crystal film placed at various locations within the unloaded cavity during microwave application. The E-field distribution within the cavity was also determined by modeling the cavity using COMSOL Multiphysics 5.1 (Fig. 1b). The E-field strength in the volume occupied by the pyrotechnic flame was estimated via dielectric heating of a 100 cm^3 vol. of water according to the National Bureau of Standards procedure [29], yielding an average electric field strength of 2.1 ± 0.1 kV/m within the antinode of interest. Samples were microwave-ignited using an electromagnetically absorbing thin film (polyester/vapor deposited aluminum film), which was placed on the top of pyrotechnics and heated until ignition. For baseline experiments (without microwave), the pyrotechnic composition was ignited directly using a hot wire ignition source.

2.4. Combustion diagnostics

A Phantom v7.0 color complementary metal-oxide semiconductor (CMOS) camera and Canon zoom lens were used to capture high-speed video of the pyrotechnic combustion (500 Hz, 10 to 100 µs exposure, Fig. 1a). To monitor the VIS/NIR spectral emission, an Ocean Optics USB4000 spectrometer (200 to 900 nm, 25 μm slit, 600 lines/mm, ~100 Hz, 10 ms integration time) was used with an OceanOptics multimode fiber (400 µm diameter, P400–0.25-SR). Light was collected onto the fiber end using a cosine corrector (OceanOptics, CC-3-UV-S) to capture a large field of view within the white (optically reflective) microwave cavity. Prior to testing, the VIS/NIR spectrometer was calibrated using a deuterium tungsten-halogen light source (OceanOptics, DH-2000-CAL) to correct for detector responsivity and achieve relative spectral irradiance measurements. Emission spectra were post-processed using MATLAB to correct for dark noise level and detector responsivity. From calibrated spectra, measures of time-integrated spectral emission were calculated as

$$E_{e,\ total}(\lambda) = \frac{1}{m_{sample}F_s}\sum_{i=1}^{n} E_e(\lambda, t_i), \tag{1}$$

Where $E_{e,\ total}(\lambda)$ is the time-integrated relative spectral irradiance per gram pyrotechnic for the entire burn (arb. units per gram), m_{sample} is the pyrotechnic article mass, F_s is the spectrometer sampling frequency, $E_e(\lambda, t_i)$ is the relative spectral irradiance, λ is wavelength, and t_i is experimental time. A measure of time-integrated emission is calculated by numerically integrating $E_{e,\ total}(\lambda)$ over all wavelengths between 400 and 880 nm. Emission outside of this spectral range suffered low signal to noise levels and was omitted from the analysis.

The dominant visible wavelengths from the pyrotechnic flame emission were calculated for comparison on a CIE 1931 chromaticity diagram. In doing so, the procedure of Ref. [30] was followed. Briefly, tristimulus values for each spectrum in the time series,

$$\begin{aligned} X_i(t_i) &= \int_{\lambda=0}^{\infty} E_e(\lambda, t_i)\bar{x}(\lambda)d\lambda \quad Y_i(t_i) \\ &= \int_{\lambda=0}^{\infty} E_e(\lambda, t_i)\bar{y}(\lambda)d\lambda \ Z_i(t_i) = \int_{\lambda=0}^{\infty} E_e(\lambda, t_i)\bar{z}(\lambda)d\lambda \end{aligned} \tag{2}$$

were calculated, where $X_i(t_i)$, $Y_i(t_i)$, and $Z_i(t_i)$ are the tristimulus values of the relative spectral irradiances in the time series, and $\bar{x}(\lambda)$, $\bar{y}(\lambda)$, and $\bar{z}(\lambda)$ are the CIE 1931 two-degree field of view color-matching functions. The chromaticity coordinates, $x_i(t_i)$ and $y_i(t_i)$ of each spectrum in the time series are then calculated as

$$x_i(t_i) = \frac{X_i(t_i)}{X_i(t_i)+Y_i(t_i)+Z_i(t_i)} \quad y_i(t_i) = \frac{Y_i(t_i)}{X_i(t_i)+Y_i(t_i)+Z_i(t_i)}. \tag{3}$$

To capture the infrared emission spectra, a Spectraline ES200 IR spectrometer (1.2 to 5.5 μm, 1320 Hz, ~0.03 μm resolution) was used. The collection angle of the spectrometer is 0.5° and captured an approximately 0.5 mm wide by 6 mm tall area at the experimental distance. This sampling volume was positioned 25 mm above the pyrotechnic sample. As such, unlike visible spectra, which are representative of entire flame emission, IR emission spectra are from a small volume above the pyrotechnic article and not representative of the entire flame. Prior to use, the IR spectrometer was calibrated using a gray body source placed at the experimental observation distance to produce measures of absolute irradiance. IR emission was post-processed in MATLAB to calculate time-integrated emission. The rise time of the E-field is expected to be short (on the order of milliseconds or less), which is much shorter than UV/VIS instrumentation that is used to assess the degree of light emission enhancement.

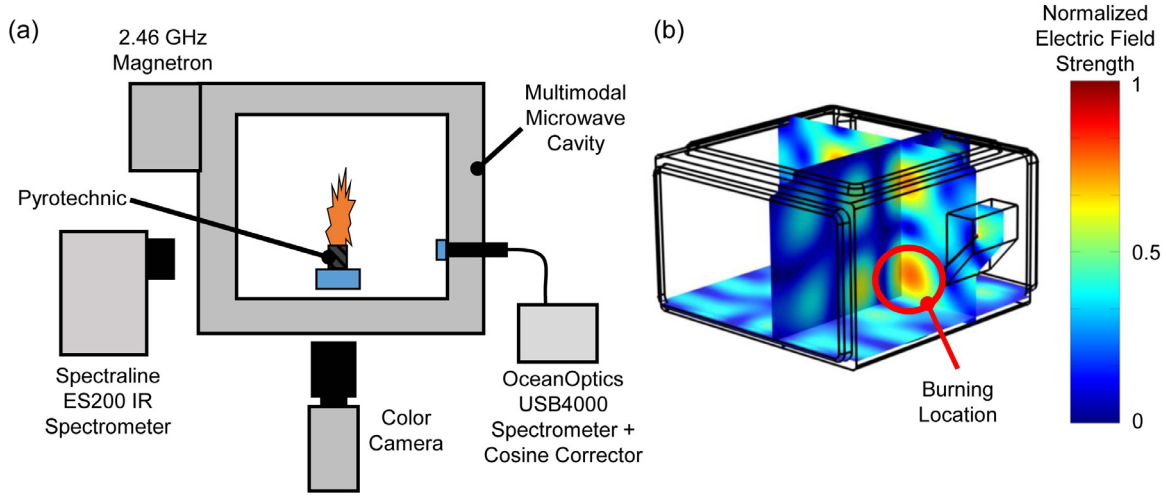

Fig. 1. (a) Schematic of the experimental setup of the microwave cavity. Experiments were monitored with a color high-speed camera and two spectrometers (VIS/NIR and IR). (b) Distribution of the mean electric field strength simulated using COMSOL within the microwave chamber. The red circle indicates the location of the pyrotechnic flame, which is located at an E-field antinode with an average field strength of 2.1 ± 0.1 kV/m in a 100 cm^3 vol. of water.

2.5. Microwave-enhanced (VIS/NIR) emission model

Comprehensive modeling of microwave-enhanced pyrotechnics is a formidable challenge. A high-fidelity approach would require coupling radiation-transfer, electric field propagation, chemically reacting fluid dynamics, and non-equilibrium electron kinetics, covering a vast range of timescales over multiple dimensions. As a first step, we introduce a collisional-radiative model with the minimum components needed to capture the proposed WMIP effect for atomic alkali emission in quasi-steady state over plasma and optical timescales ($\approx 0.5 - 50\ ns$). This requires solving a radiation transfer equation where both the emission rate and probability of radiation escape vary as a function of distance into a model plume. The emission coefficient varies according to a kinetic rate balance regulated by the local electric field strength, which in turn is determined from the penetration characteristics of an applied microwave field. The result is a spectrally-integrated solution for radiance emitted perpendicular to the plume surface. Ratios of radiance with and without applied fields are then directly compared to ratios of irradiance in experiments computed in Eq. (1).

Four key assumptions were necessary to simplify the dimensions and number of required parameters; the rationale for these assumptions are discussed in Appendix A. They are: (1) Except for alkali species, the plume is treated as a homogenous and quiescent post-combustion zone with a prescribed temperature and alkali mole fraction deviating from CEA equilibrium, with a hard interface to the ambient environment; (2) the microwave field does not significantly perturb the plume from Saha equilibrium or increase the plume temperature; (3) Planck equilibrium is maintained within the plume such that only a minor fraction of radiation escapes and is ultimately detected; and (4) the rates of alkali absorption and emission are negligible compared to kinetic pathways. As heat and mass transfer from entrained air are expected, the plume temperature T_0 and alkali mole fraction X_{alk} are left as parameters to represent the conditions for the outer layer of the plume, averaged over time and plume surface.

For a single atomic alkali transition or doublet, the resulting radiance is a convolution integral of the rate of radiant energy emission and the frequency-integrated probability of photon escape from the plume. Integrating from the plume center line ($s = L$) to the edge ($s = 0$), this takes the base form,

$$I = \int_0^L \varepsilon(s)\mathcal{T}(s)ds \tag{4}$$

where: s is the normalized plume depth described graphically in Fig. 2, I is the radiance ($Wm^{-2}sr^{-1}$) at the surface of the plume; $\varepsilon(s)$ is the volumetric emission coefficient ($Wm^{-3}sr^{-1}$) at a given depth; L is the width of the plume slab; and $\mathcal{T}(s)$ is the transmittance, or normalized probability of photon escape to $s = 0$. A sample configuration is shown in Fig. 2, where the field strength, transmittance, and emission coefficient all decline until a critical depth $s = \delta$, or skin depth, where the field effect becomes negligible.

The derivation of transmittance is described in Appendix B, which relies on the presence of resonant line broadening reviewed by de Groot and Vliet [25], and the frequency-averaged escape factors reviewed by Drawin and Emard [31]. The result depends only on the depth, s, and the wavelength λ.

$$\mathcal{T}(s) = s^{-\frac{1}{2}}\sqrt{\frac{\lambda}{4\pi^2}},\ s > \frac{\lambda}{4\pi} \tag{5}$$

For Eq. (4), the integration of $s < \lambda/4\pi$ can be neglected, as $L \gg \lambda$. The emission coefficient is obtained by

$$\varepsilon(s) = A_{21}\frac{h\nu}{4\pi}N_2 = \frac{1}{\lambda^3}\left(\frac{g_1}{g_2}\frac{2\pi e^2}{\varepsilon_0 m_e}f_{12}\right)\frac{h}{4\pi}N_2 \tag{6}$$

where A_{21} is the coefficient for spontaneous emission, g_1/g_2 is the ratio of ground to excited state degeneracies, ν is the photon frequency, f_{12} is the oscillator potential, and N_2 is the non-equilibrium excited-state alkali population. The emission coefficient for sodium and potassium doublets were computed as single transitions. For cesium, only the higher-energy transition, Cs 6P(3/2), was measured and simulated. The local N_2 population is obtained using assumption (4), which neglects emission and absorption in the steady-state rate balance

$$N_2(s) = N_1\frac{K_{M+}X_{mol} + K_{E+}(s)X_e}{K_{M-}X_{mol} + K_{E-}(s)X_e} \tag{7}$$

where N_1 is the ground state alkali density, K_{M+} and K_{M-} are the respective rate coefficients for alkali-neutral excitation and quenching, K_{E+} and K_{E-} are the same but for alkali-electron rates, X_{mol} is the mole fraction of molecular background gas, and X_e is the mole fraction of free electrons. N_1 is defined through the parameter for alkali mole fraction X_{alk}. The electron mole fraction, X_e, is obtained through Saha equilibrium, and X_{mol} is set by CEA equilibrium calculations shown in Table 1. Out of necessity, the quenching rate of

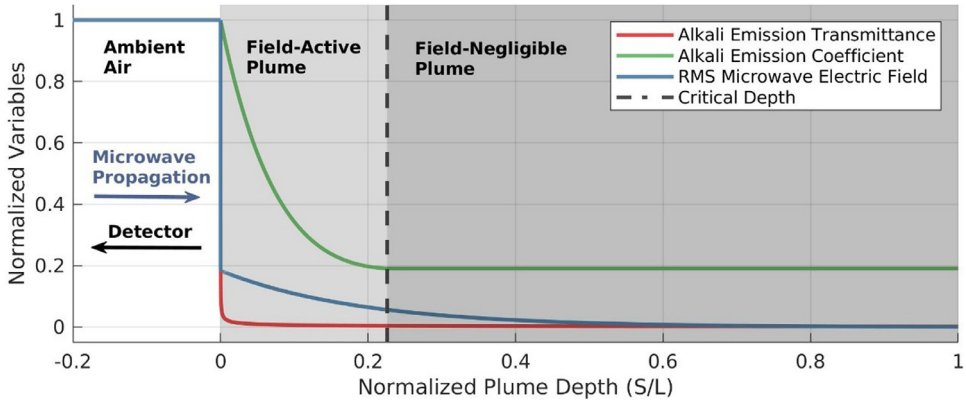

Fig. 2. Example configuration of the homogenous plume model with an incident electric field propagating left to right, perpendicular to the plume surface. Radiance is computed at surface, $s = 0$, simulating light available for detection.

Table 1
Equilibrium predictions of adiabatic flame temperature and prevalent charged/neutral combustion species of experimental compositions using CEA. Calculations assume atmospheric pressure with 10 wt.% air, and the most prevalent species are noted. For the emission model in Sections 2.5 & 3.4, the gas mixture was derived from normalizing the most prominent gases.

Formulation	$Mg/NaNO_3$/epoxy (45.6/49.4/5 wt. %)	Mg/KNO_3/epoxy (42.8/52.2/5 wt. %)	$Mg/CsNO_3$/epoxy (28.5/66.5/5 wt.%)
$T_{adiabatic}$ (K)	3088	3055	2943
Cations (mol.%)	Na^+ - 0.03	K^+ - 0.10	Cs^+ - 0.17
e^- (mol.%)	0.03	0.10	0.17
Neutral Gas-	64.8	65.4	68.6
Phase species	Na - 15.7	N_2 - 15.9	N_2 - 18.1
(mol.%)	N_2 - 15.6	Mg - 15.3	Mg - 15.1
	Mg - 13.4	K - 14.2	Cs - 12.3
	CO - 7.1	CO - 7.9	CO - 11.4
Condensed-phase species (mol.%)	$MgO_{(cr)}$−35.2	$MgO_{(cr)}$−34.5	$MgO_{(cr)}$−31.2

all molecular species is assumed to match that of molecular nitrogen, which is already a sizeable fraction of the mixtures shown in Table 1. Because all the alkali-molecule interactions are treated as alkali-nitrogen, the effect of air entrainment on Eq. (7) is contained implicitly in the free parameter X_{alk} and its relationship with X_{mol}.

At flame and pyrotechnic temperatures, the quenching rate K_{M-} approaches the thermal limit

$$K_{M-} = \sigma_A \sqrt{\frac{8k_bT_0}{\pi\,\mu_{eff}}} \tag{8}$$

where σ_A is a cross section specific to each alkali, and μ_{eff} is the effective reduced mass of the alkali species with N_2 [24]. The complementary excitation rate K_{M+} is then constrained by the requirement of detailed balance. Using Maxwell-Boltzmann statistics, an Arrhenius expression for K_{M+} can be obtained

$$K_{M+} = \left[\sigma_A \sqrt{\frac{8k_b}{\pi\,\mu_{eff}}}\frac{g_2}{g_1}\right] T_0^{\frac{1}{2}}\, \exp\left(-\frac{hc}{\lambda}\frac{1}{k_bT_0}\right). \tag{9}$$

The electron-alkali rate coefficients K_{E+} and K_{E-} are determined from the BOLSIG+ code, which uses a two-term approximation to the Boltzmann equation to solve for the non-equilibrium electron energy distribution with an applied field effects [27]. Cross-sections for equilibrium products are obtained from the LXCat database for N_2 [32], CO [33], and Mg [34], which are used to approximate non-alkali combustion products. Alkali cross sections for elastic, excitation, and ionization are obtained for sodium, potassium, and cesium [35–37]. The resulting rates are computed as functions of the reduced root-mean square (RMS) electric field (E/n_0, units of Td) and fitted to quadratic and logarithmic functions of electric field magnitude $E(s)$ once total number density inside the plume n_0 is known.

$$K_{E+} = P_1E(s)^2 + P_2E(s) + P_3, \quad K_{E-} = Q_1 + Q_2\ln(E(s)) \tag{10}$$

The microwave field solution $E(s)$ is computed using Fresnel equations for an electric field in air incident on an absorbing medium:

$$E(s) = E(0)\left[\frac{2}{1+|\widetilde{\mu_0}|}\right]\exp\left(-s\alpha_0\right) \tag{11}$$

where $E(0)$ is the incident RMS electric field magnitude, determined from the parameter for applied reduced field (E_{RMS}/n_{amb}) in the cavity outside the plume. The magnitude of the complex index of refraction $|\widetilde{\mu_0}|$ and attenuation coefficient α_0 are calculated for plume conditions using the equations for collisional plasmas listed by Laroussi [38], where electron collision frequency is estimated from BOLSIG+ results.

A complication of using the BOLSIG+ solver is that K_{E+} curve fits are typically invalid below 10 to 20 Td. This occurs when the field strength becomes negligible and thermal electrons become the dominant source of excitation. The reduced field where this transition occurs (defined as $(E/n_0)^*$), can be obtained by inspection of Eq. (10). The skin depth $s = \delta$ of this transition to a zero-field regime is found by manipulation of Eq. (11).

$$\delta = -\frac{1}{\alpha_0} ln\left[\frac{(E/n_0)^*}{(E(0)/n_{amb})}\left(\frac{T_{amb}}{T_0}\right)\left(\frac{1+|\widetilde{\mu_0}|}{2}\right)\right] \tag{12}$$

Where the minimum skin depth for is $\delta = \lambda/4\pi \approx 0$. Then Eq. (4) for total radiance can be solved piecemeal with Eqs. (5)-(12) by isolating the zero-field emission term $\varepsilon(\delta)$:

$$I = \int_{\lambda/4\pi}^{\delta} \varepsilon(s)\mathcal{T}(s)ds + \varepsilon(\delta)\int_{\delta}^{L}\mathcal{T}(s)ds\,. \tag{13}$$

Finally, the ratio of radiance with and without microwave application can be obtained as

$$R = \frac{\int_{\lambda/4\pi}^{\delta}\varepsilon(s)\mathcal{T}(s)ds + \varepsilon(\delta)\int_{\delta}^{L}\mathcal{T}(s)ds}{\varepsilon(0)\int_{\lambda/4\pi}^{L}\mathcal{T}(s)ds}, \tag{14}$$

Table 2
Electronic transitions of prevalent gas-phase atoms observed in Mg/alkali-nitrate flames [39].

Species	Wavelength (nm)	Transition	Spontaneous Emission Rate, A_{ki} (10^8 s^{-1})	Transition Energy (eV)
Cs I	852.1	6s-6p	0.328	1.455
Na I	819.1	3p-3d	0.495	1.514
K I	767.6	4s-4p	0.385	1.615
Na I	589.2	3s-3p	0.615	2.104
Mg I	517.8	3s3p-3s4s	1.040	2.394

where the primary unknown parameters are E_{RMS}/n_{amb}, T_0, and X_{alk}.

3. Results and discussion

3.1. Equilibrium chemical calculation

The predicted adiabatic flame temperature ($T_{adiabatic}$) and prevalent ion and neutral product species of the three pyrotechnic formulations investigated are shown in Table 1. Stoichiometric formulations of Mg/alkali nitrate systems were found to maximize predicted free electron and ion concentration due to high flame temperature. In addition to maximizing free electron populations, the predicted equilibrium products contain several neutral atomic gas species with low ionization and low energy electron transitions (e.g., Na, K, Cs, Mg). From the list of major atomic gas-phase species, transitions with the highest spontaneous emission rates are listed in Table 2. Only Mg I (517.8 nm) and Na I (589.2 nm) are transitions with high spontaneous emission rates that are in the visible spectrum, while Cs I (852.1 nm) and K I (767.6 nm) are transitions with high spontaneous emission rates in the NIR spectrum. Equilibrium calculations indicate that combustion products at adiabatic flame temperature consist of both vapor-phase and condensed-phase species. Contrary to gas phase species, condensed phase species are expected to undergo sensible enthalpy change proportional to species' dielectric loss characteristics when subjected to microwave illumination. The product composition also consists of 1.0 to 3.1 mol.% vapor phase MgO and 31.2 to 35.2 mol.% $MgO_{(cr)}$. As discussed previously, the presence of both condensed phase and gas phase species are important in consideration electric field interaction, as energy absorption by condensed phase is typically by dielectric modes and energy absorption by gas phase species typically occurs by electronic modes. The major neutral gas-phase species shown in Table 1 were used in the 1-D microwave-enhanced emission model.

3.2. Microwave effects on flame structure

Image sequences (Fig. 3) and the supplemental video show an example of the effect of modulated microwave illumination on the flame structure of a Mg/KNO_3/epoxy pyrotechnic. Without microwave illumination, the primary flame intensity varies with a visible flame height between 1 and 1.5 cm. With microwave illumination, flame emission and size modulate in phase with the application of electromagnetic field (60 Hz duty cycle). During the microwave illumination period emission intensity increases and the flame volume grows. The emission region grows to 3 to 4 cm in height from the burning surface. The emission enhancement of the flame is expected, in part, from the high alkali metal content of the formulations, which results in emission from low-lying electronic states [8–12]. For all formulations tested, microwave field application increased both the visible flame volume and emission intensity.

For all pyrotechnic systems evaluated, sustained visible light emission after pyrotechnic flame extinguishment was also observed. The resulting post-combustion emission, shown in Fig. 4, occurs near the top of the multimodal cavity at a probable E-field antinode. The post-combustion products continue to emit periodically in phase with the 60 Hz microwave field modulation for long durations of time (~10 s or longer after pyrotechnic extinguishment).

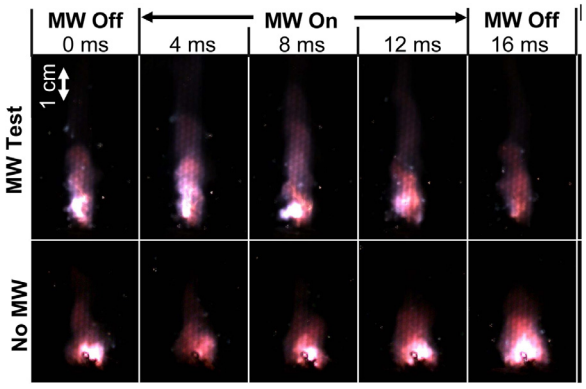

Fig. 3. Image sequence of the Mg/KNO_3/epoxy pyrotechnic combustion with (top) and without (bottom) microwave illumination, where the microwave field is sinusoidally modulated at 60 Hz. During the microwave illumination period, flame growth and emission increase can be seen above the main flame. Both images are taken with the same exposure and frame rate (20 μs, 500 Hz).

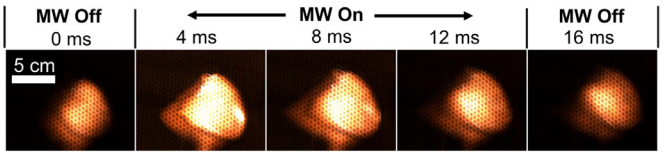

Fig. 4. Image sequence of the microwave field enhancement of Mg/$NaNO_3$/epoxy post-combustion products where the microwave field is sinusoidally modulated at 60 Hz. The pyrotechnic article is out of view in these images.

3.3. VIS/NIR spectral emission enhancement

Time-resolved VIS/NIR emission spectra from combustion of Mg/$NaNO_3$/epoxy pyrotechnics are shown in Fig. 5. As compared to non-microwave illuminated conditions, significant atomic emission enhancement is detected. For the Mg/$NaNO_3$/epoxy system, enhanced emission was observed at the expected atomic emission lines at 589 nm (Na I, 3p-3 s), 819 nm (Na I, 3d-3p), 568 nm (Na I, 4d-3p), 615 nm (Na I, 5s-3p), 670 nm (Li I, 2p-2 s), 766 nm (K I, 4p-4 s), and 850 nm (Cs I 6p(3/2)−6 s). Emission from Li I, K I, and Cs I seen in the Mg/$NaNO_3$/epoxy system is likely due to contamination in the microwave cavity from prior experiments.

The typical combustion duration for each pyrotechnic experiment was approximately four seconds with microwave illumination and five seconds without microwave illumination. Emission from the sustained post-combustion plasma can be seen in the right panel of Fig. 5 between experiment times of approximately five to fifteen seconds. The post-combustion emission from the Mg/$NaNO_3$/epoxy system is primarily from atomic sodium emission (Na I, 3p-3 s). This effect was also observed in the other two

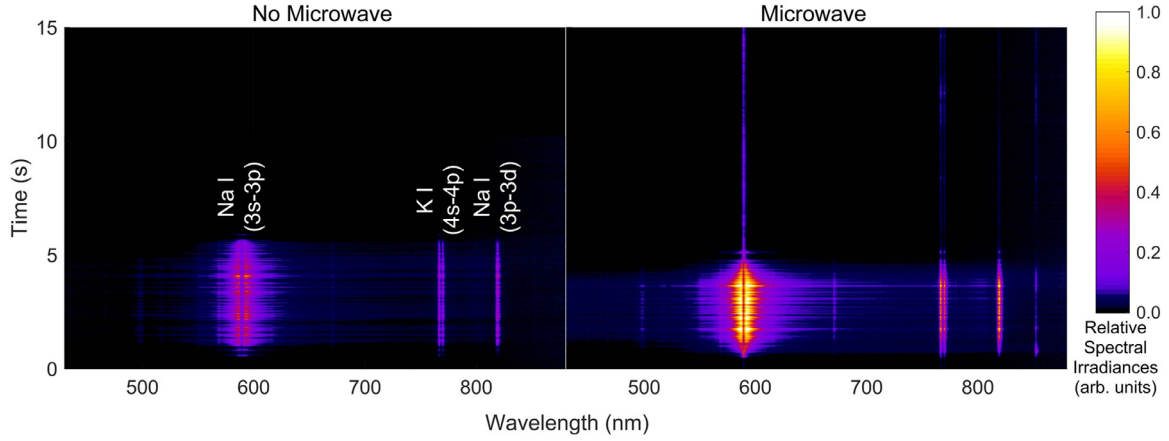

Fig. 5. Time histories of $Mg/NaNO_3$/epoxy pyrotechnic combustion emission from the baseline condition (no microwave, left) and with microwave illumination (right). Continuous emission from the atomic species long after pyrotechnic extinguishment can be seen (~5–15 s) as a result of microwave illumination of combustion products. Spectra intensities are normalized based on detector exposure time such that intensities of the two experimental trials are relative to each other.

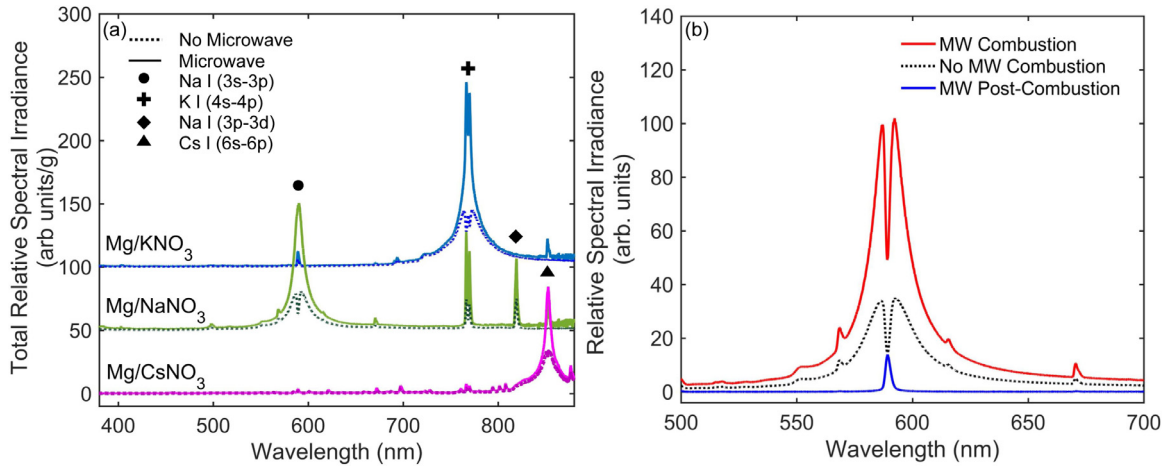

Fig. 6. (a) Time-integrated, relative spectral irradiance of each pyrotechnic during combustion, both with and without microwave illumination in arb. units per gram pyrotechnic reagent. Species responsible for strong electronic transition features observed in VIS/NIR emission are noted. Increased emission from atomic transitions can be seen with illumination. Some atomic emission enhancement is also observed from contaminant alkali species that are present in the multimode microwave cavity which are excited during combustion and microwave illumination (e.g., Li, Na, K, and Cs). Spectra intensities are all relative and spectra from each formulation are offset for clarity. (b) Typical emission spectral features from $Mg/NaNO_3$/epoxy pyrotechnic combustion with and without microwave.

alkali-nitrate pyrotechnic formulations, but to a lesser extent. In all formulations, atomic emission enhancement primarily occurs from the lowest energy electronic transition of the respective dopant alkali atom. By inspection of Eqs. (7) and (9), it is apparent that without substantial electron-alkali excitation or continual heat transfer to maintain plume temperature, sustaining non-equilibrium excited-state alkali population N_2 is not possible. The long-duration sustained emission is therefore strong evidence that WMIP is directly responsible for generating increased excited-state alkali species, especially for post-combustion periods where the ratio of intensities is nearly infinite.

Microwave illumination of other Mg/alkali nitrate pyrotechnic systems resulted in atomic emission enhancements similar to $Mg/NaNO_3$ formulations. These results are summarized in time-integrated, VIS/NIR spectral irradiance measures of the three pyrotechnic formulations (Fig. 6a). Similar to the sodium nitrate-based formulation, the majority of emission enhancement observed in both the potassium and cesium nitrate pyrotechnic formulations was due to enhanced emission from low energy electronic transitions from excited state alkali neutrals (Mg/KNO_3/epoxy: K I, 4p-4 s, and $Mg/CsNO_3$/epoxy: Cs I, 6p(3/2)−6 s). As expected, resonant broadening and self-absorption of the alkali resonance-line continuum is apparent (Fig. 6) without microwave illumination. Self-absorption also occurs in microwave illuminated emission from all formulations, though is not apparent in time-integrated spectra of Fig. 6a due to the additional emission contribution of the microwave-supported plasma that occurs after pyrotechnic extinguishment. Self-absorption and resonance broadening can be more clearly seen in typical time-resolved emission spectra from $Mg/NaNO_3$/epoxy (Fig. 6b).

Other, lower intensity peaks are also observed that correspond to additional electronic transitions of the alkali metals. These emission features are noted in Fig. 6a. Some atomic emission enhancement is also observed from contaminant alkali species that are present in the multimode microwave cavity which are excited during combustion and microwave illumination (e.g., Li, Na, K, and Cs). Even though equilibrium-predicted Mg populations are similar to those of alkali metals and spontaneous emission rates are even higher, little Mg I emission is observed for conditions with and without microwave illumination at the two transitions of interest (383.5 nm, 3s3p-3s3d and 517.8 nm, 3s3p-3s4s, shown in Table 2). We postulate that the higher transition energy of Mg I and shorter lifetime of Mg vapor due to oxidization contribute to lower Mg I emission. Additionally, little gray body continuum emission enhancement is observed in VIS/NIR spectra even with high predicted concentration of condensed phase MgO; it is expected that within

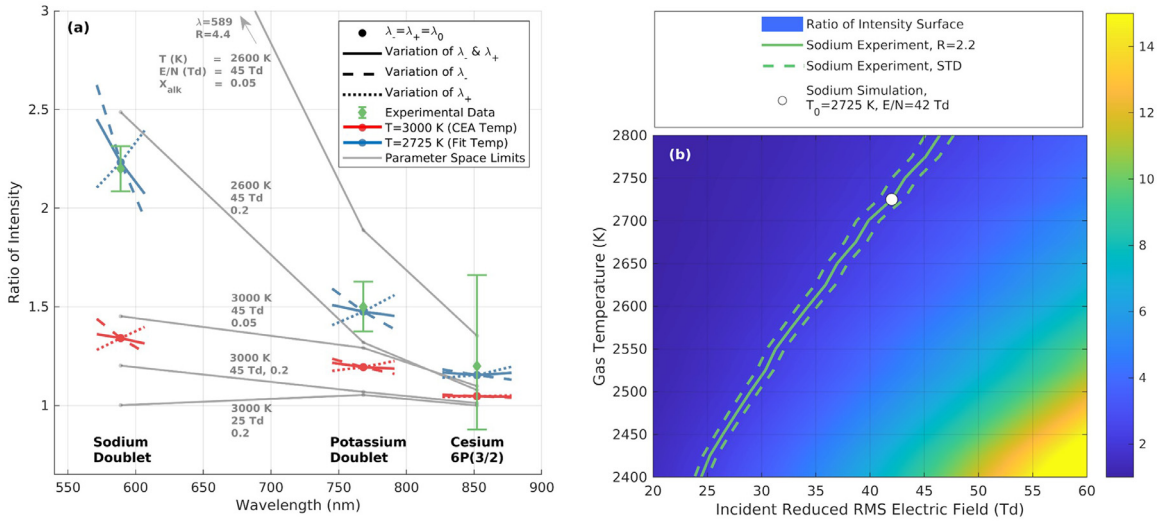

Fig. 7. (a) Model results for ratio of radiance with and without applied microwave is shown (Eq. (14)). A best fit solution was found for incident RMS field strength of 42 Td, alkali mole fraction of 6 vol.%, and temperature of 2725 K (blue). A high temperature case representative of CEA equilibrium conditions is also shown (red). Each case is plotted at line center λ_{21}, with perturbations in wavelength showing the local sensitivity from several terms in Eqs. (3)-(14) producing positive change with wavelength (λ_+), the single term K_{M+} producing negative change (λ_-), and total change (λ_- and λ_+). Experimental frequency-integrated irradiance ratios are also plotted, with error bars representing the standard deviation of three trials (green). Lastly, five of a set of eight simulations are shown covering the practical limits across the three major parameters (gray). (b) The enhancement ratio in (a) is computed for sodium over a range of temperature and field strength values. Contours representing the corresponding experimental value plus/minus one standard deviation are overlaid with simulations, along with the fitted temperature and field strength.

the combustion plume, microwave absorption primarily occurs to the gas phase plasma.

For pyrotechnic formulations investigated in this effort, microwave energy is expected to be preferentially absorbed electronically to the gas-phase through inelastic electron-neutral collisions rather than dielectrically by the condensed-phase reactants. Some dielectric heating of the condensed phase does occur, however, as demonstrated by microwave-based auto-ignition of pyrotechnic articles which can be achieved after ~40 s of microwave illumination. Assuming pyrotechnic article microwave heating is spatially uniform and assuming autoignition occurs between 467 °C and 565 °C [40], and neglecting convective losses, we estimate the average microwave absorption of condensed phase reactants is 6.0 W to 7.3 W. Much of the condensed phase reactant heating is expected to be a result of microwave loss in the metal nitrate. Studies on microwave sintering of Mg particles have found Mg heating to be slow (17.1 K/min, 1.0 kW multimodal cavity) [41]. The dielectric loss of the metal nitrate reagents used in this effort are expected to be higher than Mg particle heating, as the microwave heating rate of ammonium nitrate to ignition has been reported in literature to be on the order of minutes (178.8 K/min, 1.1 kW single mode cavity) [21].

3.4. VIS/NIR emission enhancement mechanism

In order to compare the proposed model to experimental results, integration of the spectral irradiance from 400 to 880 nm in Fig. 6 was used to produce an estimate of the ratio of time-integrated irradiance with and without microwave exposure (green dots, Fig. 7a). Surprisingly, this emission enhancement was found to correlate positively with shorter wavelength, higher energy, transitions. The pyrotechnic with the highest alkali transition energy, $NaNO_3$, yielded a ratio of 2.2, or 120% increase in time-integrated irradiance when microwaves were applied. Potassium and cesium cases experienced an average of 50% and 20% irradiance enhancements, respectively. These results were compared directly to simulated ratios of radiance computed using Eq. (14).

Given the challenges in grounding simulation parameters (gas temperature T_0, field strength E_{RMS}/n_{amb}, and alkali mole fraction X_{alk}) firmly in measurements, we instead show that a suitable parameter set exists that can replicate all three alkali enhancement ratios simultaneously. Such a case was found for reduced field strength of 42 Td, plume temperature of 2725 K, and an alkali fraction of 6 vol.%, and is within experimental margin of error for all alkali species (blue dots, Fig. 7a). This serves as an initial demonstration of consistency for the WMIP model for pyrotechnic emission enhancement. For comparison purposes, we also present calculations for the same case but with a gas temperature near CEA equilibrium temperatures (red dots, Fig. 7a).

As the reliance of Eq. (14) on wavelength (or transition energy) could not be obtained by simple inspection of Eqs. (4)-(13), the various wavelength dependencies within the model were artificially perturbed from line center λ_{21} to identify the dominant terms (solid and broken lines, Fig. 7a). To simplify the results, wavelength parameters λ_- and λ_+ were used to group terms with similar effects on emission enhancement. Specifically, the λ_- group followed the experimental trend of diminishing enhancement with increasing wavelength, whereas λ_+ opposed it. From initial calculations, it was immediately clear that only the wavelength dependence of K_{M+} (Eq. (9)) contributed to λ_-. The λ_+ term contained all other wavelength dependencies, including: (1) calculation of transmittance via optical depth (Eq. (5)), (2) spontaneous emission coefficient (Eq. (6)), and (3) cross-sections for electron-alkali excitation, where cross-section curves were artificially shifted in energy space to correspond to an alternate transition energy ($\Delta\varepsilon = hc/\lambda_+$). The procedure for altering cross-sections does not account for hypothetical changes in cross-section shape, however the curves are roughly comparable across alkali species, independent of transition energy. Finally, both λ_+ and λ_- were also varied together to show the cumulative sensitivity to wavelength.

With the results displayed in Fig. 7a, a preliminary hypothesis can be constructed to explain why WMIP emission enhancement in the VIS/NIR range is maximized for alkali species with shorter wavelength (higher-energy) transitions. Photons with shorter wavelengths (Eq. (5)) have a diminished probability of escape, which restricts the effect of any enhancement. Likewise, alkali species with an increased energy threshold for electron-alkali excitation collisions K_{E+} plainly counters the ability of an electric

field to promote non-equilibrium emitters. The same can be said for emission coefficient, which increases the baseline emission rate independent of the microwave field by the third power of wavelength (Eq. (6)). Despite these effects, the model for enhancement is most sensitive to neutral-alkali excitation rate K_{M+} (Eq. (9)), which falls off exponentially for transition energies above the gas thermal energy ($hc/\lambda > k_b T_0 \approx 0.25$ eV). The net effect is that K_{M+} falls off faster with lower wavelength than K_{E+} (whose rate is field-driven and not limited by equilibrium Maxwell-Boltzmann statistics). Hence, K_{E+} develops a proportionally larger effect than K_{M+} on emitter population N_2 (and hence, emission rate ε) through Eq. (7).

To further reinforce that this result is independent of parameter selection, simulations at line-center wavelength were conducted across a wide domain of parameter space ($T_0 = [2400,\ 3000]K$, $X_{alk} = [0.05,\ 0.2]$, E_{RMS}/n_{amb},=[20, 45] Td), and five notable examples of the eight combinations were plotted in the background of Fig. 7a. These show that the general trend between the alkalis hold for all but one case. The extraneous limit with very low enhancement was a result of strong shielding properties ($T_0 = 3000\ K$, $X_{alk} = 0.20$, E_{RMS}/n_{amb},=20 Td). To show the parameter space in more detail, the intensity ratio solution computed in Fig. 7a for sodium was expanded in Fig. 7b over a broad range of temperature and field strength values (matching the above limits, but with $X_{alk} = 0.06$). Contours representing the experimental mean and standard deviation are shown, identifying a locus of temperature and field strength values that provide high-quality fits. This demonstrates that the enhancement for sodium is consistent with relatively weak microwave fields (<30 Td), provided the plume temperature is significantly lower than equilibrium temperature ($T_0 \ll 3000\ K$). This is also consistent with the intense enhancement observed during the cool post-combustion time period shown in Fig. 5, where a large reduction in thermal energy, $k_b T_0$, in Eq. (9) can diminish K_{M+}, a change consistent with a shift to a higher energy (lower wavelength) transition.

While the proposed WMIP model appears consistent with experiments, it is not free of limitations. Most immediate to the wavelength sensitivity analysis, the evaluation of rate coefficients may be incomplete, as: (1) the wavelength dependence of alkali cross-sections are only crudely approximated; and (2) the two-term Boltzmann approximation may carry significant error for high-pressure molecular discharges. These limitations require further review. For the model, the lack of a well-prescribed temperature distribution, field strength, and alkali mole-fraction prevents rigorous validation, and the homogenous plume assumption must be tested against spatially-resolved temperature and radiance data. These limitations reinforce the need for further investigation with more capable numerical methods and improved diagnostics.

3.5. Microwave effects on luminosity and chromaticity

Emission from the Mg/$NaNO_3$/epoxy time-series spectra were plotted on chromaticity diagrams (Fig. 8) for three conditions: baseline pyrotechnic combustion without microwave illumination, pyrotechnic combustion with microwave illumination, and microwave illumination of post-combustion products. Figure 8 shows high color purity for all three conditions. Emission for all three conditions is dominated by the 589 nm Na I emission (3p-3 s transition, Fig. 5) and Fig. 8 furthers shows that all three conditions produce light emission of similar dominant wavelength. With respect to the subtle trends in emission, with microwave illumination, emission becomes more monochromatic and follows the 589 nm emission line. This effect is particularly evident in emission post-extinguishment. Color purity of the post-combustion plasma light emission is found to vary more than either of the other two conditions, which may be due to the low intensity of post-combustion emission, and amplification of noise during calculation of the dominant color (spectrometer integration time during experiments was optimized for sampling during the combustion period rather than the post-combustion period). The chromaticity analysis of the Mg/$NaNO_3$/epoxy formulation suggests overall that emission color of the pyrotechnic produced from microwave enhancement is similar to that of the baseline pyrotechnic emission. The potassium and cesium-based systems were not analyzed because their primary emission bands are outside the visible spectrum.

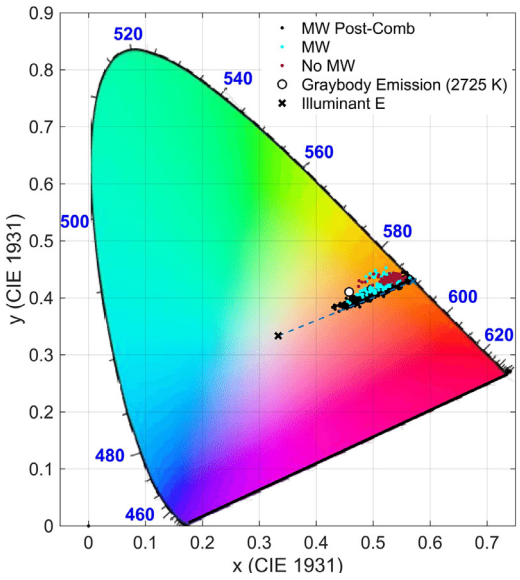

Fig. 8. CIE 1931 chromaticity diagram showing time-resolved color and purity of emission from Mg/$NaNO_3$/epoxy pyrotechnics (1) without microwave illumination, (2) with microwave illumination, and (3) emission acquired from microwave illumination of combustion products post-extinguishment. Graybody emission at 2725 K and the Illuminant E point is indicated on the diagram. The dash line represents dominant wavelength of 589.2 nm of varying color purity.

3.6. IR emission enhancement

Measures of time-averaged IR spectral irradiance of each alkali-nitrate formulation (Fig. 9) showed that emission enhancement resulting from microwave illumination of the three formulations extended beyond the visible spectrum and into the IR. Specifically, enhancement of emission from Na I (0.947 μm), K I (1.048, 1.177, and 1.415 μm), and Cs I (1.358, 1.469, 3.010, 3.490, and 3.614 μm) electronic transitions were observed. Additionally, slight emission enhancement of the CO_2 (~4.2 to 4.8 μm) and H_2O (~2.5 to 3.0 μm) IR emission bands were observed for all formulations.

Similar to the visible enhancement results (Fig. 6), little gray body continuum emission enhancement was observed in the near infrared as a result of microwave illumination. This is in contrast to the high concentration of equilibrium-predicted condensed-phase products within the flame (Table 1, 31.2 to 35.2 mol.%) and the high equilibrium flame temperatures of compositions (2943 to 3088 K). In similar studies involving microwave illumination of aluminized AP composite propellants containing $NaNO_3$ dopant [14], continuum emission enhancement of alumina products from aluminum agglomerate diffusion flames was observed as a result of the exponentially temperature-dependent increase in aluminum oxide microwave absorptivity (i.e. microwave loss tangent) that has been observed by others [15]. The high temperature increase in microwave absorptivity, referred to as 'thermal runaway' in microwave sintering literature, is observed in many ceramics as a result of a shift in heating mechanism from dielectric at low

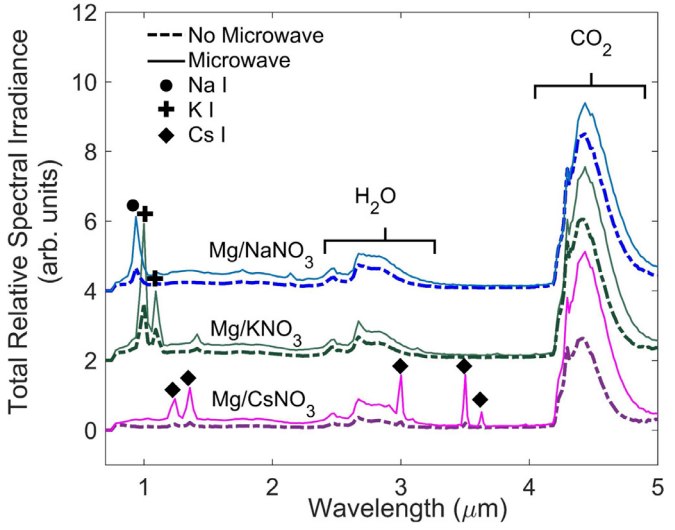

Fig. 9. Time-integrated, infrared total spectral irradiance of each Mg/alkali nitrate/epoxy pyrotechnic with and without microwave illumination. Species of significant electronic atomic and molecular emission enhancements observed are noted. Irradiance values for each formulation are offset for presentation purposes.

temperatures to eddy current heating at high temperature due to increased charge mobility at higher temperatures [42]. In the aforementioned propellant study, aluminum oxide exists in liquid phase, where its acts as an ionic conductor due to enhanced charge mobility [43]. Consequently, application of an electric field to liquid aluminum oxide can result in more efficient energy absorption and conversion to heat. Conversely for the MgO products within pyrotechnic flames of this study, the MgO remains in solid phase due adiabatic flame temperatures that are lower than the melting point of MgO. Dielectric absorption of solid MgO products may be inefficient at pyrotechnic flame temperatures, as little continuum emission enhancement is observed.

4. Conclusion

This effort explores the effects of microwave illumination on the irradiance and color of Mg/alkali metal nitrate pyrotechnic flames, providing evidence that classic pyrotechnic formulations for colored illumination can be manipulated with plasma-assisted combustion techniques. Despite initial concerns that microwaves cannot penetrate pyrotechnic plumes, microwave exposure resulted in spectrally integrated VIS/NIR irradiance enhancement within the 400 to 880 nm range of up to 120%. While recording little effect on overall color, enhancement of low-energy alkali transitions was observed long after extinguishment of the pyrotechnic through continued microwave illumination of the combustion products. Some emission enhancement from molecular species were also observed in the IR wavelengths.

Additionally, a working hypothesis was presented for gas-phase alkali emission enhancement through generation of weak microwave-induced plasma (WMIP). A preliminary model was introduced that uses this hypothesis to predict average radiance improvement in pyrotechnics, with results showing that a single temperature, field strength, and alkali density combination can be used to model experimental enhancement for all three alkali-nitrate pyrotechnics at once. Additional modeling results demonstrated that the experimental trend of increasing enhancement at lower wavelengths was broadly reproduced, independent of parameter selection. These findings can be parsimoniously explained by the rate balance equations for the excited-state alkali population, which suggests that the molecular excitation of alkali atoms by background gas is exponentially reduced at lower wavelengths (Eq. (9)), augmenting the effect of applied electric fields. This dependency may also explain why cool combustion products can be favorably reilluminated with microwave fields. These results support, but do not confirm, the WMIP hypothesis; more precise measurements are needed. Advances in modeling techniques are required to account for spectral dependence, plume inhomogeneity, and coupling to chemical and fluid dynamics. Lastly, the 2016 release of BOLSIG+ was used to obtain these results; preliminary tests with the 2019 version indicated similar results can be obtained with slightly lower field strengths.

Overall, this study investigates the ability to use microwave frequency radiation to increase flame irradiance and augment flame structure of an alkali-containing pyrotechnic without significantly altering flame color. These findings have implications for development of increased brightness emitters, improved pyrotechnic light emission efficiency, advanced pyrotechnic strobes, and development of on-command tuneable light emission pyrotechnics that may enable multi-role use, simplify pyrotechnic supply and load-out, and enable new pyrotechnic functionalities. The use of high strength E-fields to enable 'smart' pyrotechnics admittedly adds an additional layer of complexity to application. However, advances in microwave directed energy weapons and recent deployment of such systems will likely be synergistic in enabling microwave 'smart' pyrotechnics.

Declaration of Competing Interest

The authors declare that they have no known competing financial interests or personal relationships that could have appeared to influence the work reported in this paper.

Acknowledgments

The authors wish to acknowledge financial support from SERDP WP19-1163 under the direction of Dr. Robin Nissan, the NSWC-Crane Naval Innovative Science and Engineering Program, and the Air Force Office of Scientific Research (FA9550-15-1-0195 and FA9550-17-1-0167) under the direction of Dr. Mitat Birkan. SJB wishes to acknowledge support from the Iowa State University Alliance for Graduate Education and the Professoriate program and the NASA Iowa Space Grant Consortium (NASA Award No. NNX16AL88H).

Supplementary materials

Supplementary material associated with this article can be found, in the online version, at doi:10.1016/j.combustflame.2020.11.005.

References

[1] W. Meyerriecks, K.L. Kosanke, Color values and spectra of the principal emitters in colored flames, J. Pyrotech. 18 (2003) 1–22.
[2] J.J. Sabatini, A.V. Nagori, G. Chen, P. Chu, R. Damavarapu, T.M. Klapötke, High--nitrogen-based pyrotechnics: longer- and brighter-burning, perchlorate-free, red-light illuminants for military and civilian applications, Chem. A Eur. J. 18 (2012) 628–631.
[3] Y. Ju, W. Sun, Plasma assisted combustion: dynamics and chemistry, Prog. Energy Combust. Sci. 48 (2015) 21–83.
[4] A. Starikovskiy, Physics and chemistry of plasma-assisted combustion, Philos. Trans. R. Soc. Lond. A Math. Phys. Eng. Sci. 373 (2015) 1–8.
[5] T. Ombrello, Y. Ju, Kinetic ignition enhancement of H2 versus fuel-blended air diffusion flames using nonequilibrium plasma, IEEE Trans. Plasma Sci. 36 (2008) 2924.
[6] T. Ombrello, Y. Ju, A. Fridman, Kinetic ignition enhancement of diffusion flames by nonequilibrium magnetic gliding arc plasma, AIAA J. 46 (2008) 2424–2433.
[7] E. Mintoussov, S. Pancheshnyi, A. Starikovskii, Propane-air flame control by non-equilibrium low-temperature pulsed nanosecond barrier discharge, 42nd AIAA Aerospace Sciences Meeting and Exhibit, 2004.

[8] B.E. Douda, R.M. Blunt, E.J. Bair, Visible radiation from illuminating-flare flames: strong emission features*†, J. Opt. Soc. Am. 60 (1970) 1116.
[9] J.E. Tanner, A Mathematical Model of Flare Plume Combustion and Radiation, Naval Weapons Support Center, Crane, IN, USA, 1975 Report No. NWSC/CR/RDTR-9.
[10] D.R. Dillehay, Resonant Line Broadening of Alkali Metals in Pyrotechnic Flames, Clayton University, 1983.
[11] H. Webster, J.E. Tanner, B.E. Douda, Theoretical Light Yields from Illuminating Flare Compositions, Naval Weapons Support Center, Crane, IN, USA, 1973 Report No. 253.
[12] B.E. Douda, E.J. Bair, Radiative transfer model of a pyrotechnic flame, J. Quant. Spectrosc. Radiat. Transf. 14 (1974) 1091–1105.
[13] R.G. Gann, F. Kaufman, M.A. Biondi, Interferometric study of the chemiluminescent excitation of sodium by active nitrogen, Chem. Phys. Lett. 16 (1972) 380–384.
[14] S.J. Barkley, K. Zhu, J.E. Lynch, J.B. Michael, T.R. Sippel, Microwave plasma enhancement of multiphase flames : on-demand control of solid propellant burning rate, Combust. Flame 199 (2019) 14–23.
[15] W.H. Sutton, Microwave processing of ceramic materials, Am. Ceram. Soc. Bull. 68 (1989) 376.
[16] M. Gupta, W.W.L. Eugene, Microwaves and Metals, John Wiley & Sons, Ltd, Singapore, 2011.
[17] K.I. Rybakov, E.A. Olevsky, E.V. K.rikun, Microwave sintering: fundamentals and modeling, J. Am. Ceram. Soc. 96 (2013) 1003–1020.
[18] C.A. Crane, M.L. Pantoya, B.L. Weeks, M. Saed, The effects of particle size on microwave heating of metal and metal oxide powders, Powder Technol. 256 (2014) 113–117.
[19] A.L. Higginbotham Duque, W.L. Perry, C.M. Anderson-Cook, Complex microwave permittivity of secondary high explosives, Propellants Explos. Pyrotech. 39 (2014) 275–283.
[20] M.E. Daily, B.B. Glover, S.F. Son, L.J. Groven, X-band microwave properties and ignition predictions of neat explosives, Propellants Explos. Pyrotech. 38 (2013) 810–817.
[21] K. Hasue, M. Tanabe, N. Watanabe, S. Nakahara, F. Okada, A. Iwama, Initiation of some energetic materials by microwave heating, Propellants Explos. Pyrotech. 15 (1990) 181–186.
[22] E. Vargas, M.L. Pantoya, M.A. Saed, B.L. Weeks, Advanced susceptors for microwave heating of energetic materials, Mater. Des. 90 (2016) 47–53.
[23] C.A. Crane, M.L. Pantoya, B.L. Weeks, Investigating the trade-offs of microwave susceptors in energetic composites: microwave heating versus combustion performance, J. Appl. Phys. 115 (2014) 1–6.
[24] P.L. Lijnse, Electronic-excitation transfer collisions in flames-VI. Interpretation of the temperature dependence of alkali-quenching by N2 and general conclusions about the energy transfer mechanism, J. Quant. Spectrosc. Radiat. Transf. 14 (1974) 1143–1155.
[25] J.J. de Groot, J.A.J.M. van Vliet, The High-Pressure Sodium Lamp, Macmillan Education, London, 1986.
[26] J.A.M. van der Mullen, Excitation equilibria in plasmas; a classification, Phys. Rep. 191 (1990) 109–220.
[27] G.J.M. Hagelaar, L.C. Pitchford, Solving the Boltzmann equation to obtain electron transport coefficients and rate coefficients for fluid models, Plasma Sources Sci. Technol. 14 (2005) 722–733.
[28] S. Gordon, B.J. McBride, Computer Program for Calculation Complex Chemical Equilibrium Compositions and Applications: I. Analysis, NASA Lewis Research Center, 1994 Reference Publication No. RP-1311.
[29] O.B. Laug, Evaluation of A Test Method for Measuring Microwave Oven Cooking Efficiency, Report No. NBSIR 77-1387, National Bureau of Standards, Washington, D.C., USA, 1977.
[30] D. Malacara, Color vision and colorimetry: theory and applications, Color Res. Appl. 28 (2003) 77–78.
[31] H.W. Drawin, F. Emard, Optical escape factors for bound-bound and free-bound radiation from plasmas Pt 1, Beitr. Plasmaphys. 13 (1973) 143–168.
[32] Biagi database, www.lxcat.net, 2020.
[33] IST-Lisbon database, www.lxcat.net, 2020.
[34] Phelps database, www.lxcat.net, 2020.
[35] K. Igenbergs, J. Schweinzer, I. Bray, D. Bridi, F. Aumayr, Database for inelastic collisions of sodium atoms with electrons, protons, and multiply charged ions, At. Data Nucl. Data Tables 94 (2008) 981–1014.
[36] K. Ratnavelu, W.E. Ong, Electron and positron scattering from atomic potassium, Eur. Phys. J. D 64 (2011) 269–285.
[37] O. Zatsarinny, K. Bartschat, N.Y. Babaeva, M.J. Kushner, Electron collisions with cesium atoms-benchmark calculations and application to modeling an excimer-pumped alkali laser, Plasma Sources Sci. Technol. 23 (2014) 35011.
[38] M. Laroussi, Interaction of microwaves with atmospheric pressure plasmas, Int. J. Infrared Millim. Waves 16 (1995) 2069–2083.
[39] A. Kramida, Y. Ralchenko, J. Reader, NIST ASD Team, NIST atomic spectra database lines form, NIST At. spectra database (Ver. 5.2) (2018) Available: http://physics.nist.gov/asd.
[40] H. Singh, M.R. Somayajulu, R. Bhaskara Rao, A study on combustion behavior of magnesium-sodium nitrate binary mixtures, Combust. Flame 76 (1989) 57–61.
[41] J.W. Walkiewicz, G. Kazonich, S.L. McGill, Microwave heating characteristics of selected minerals and compounds, Miner. Metall. Process. 5 (1988) 39–42.
[42] Y.V. B.ykov, K.I. Rybakov, V.E. Semenov, High-temperature microwave processing, J. Phys. D Appl. Phys. 34 (2001) R55–R75.
[43] H. Fay, The electrical conductivity of liquid Al2O3 (molten corundum and ruby), J. Phys. Chem. 70 (1966) 890–893.